An investigation of separation near corner points in transonic flow

By İBRAHİM TÜRKYILMAZ

Department of Mathematics, Arts and Science Faculty, Çanakkale Onsekiz Mart University,
17100 Çanakkale, Turkey

The incipient separation from a corner in steady two-dimensional transonic flow is studied based on viscous–inviscid interaction at high Reynolds number. Of particular interest is the investigation of the dependence of the critical deflection angle (when a well-attached flow turns into a separated flow) on the Kármán–Guderley parameter which characterizes the local flow field. In accordance with the procedure adopted, the analysis of the flow starts with the analysis of the boundary layer and then the solution of the Kármán–Guderley equation describing the inviscid part of the flow near the corner point is investigated. The analysis of the inviscid transonic flow is performed based on the hodograph method and new solutions are obtained corresponding to the present flow topologies. In these solutions, the transonic flow appears to be subsonic everywhere except at the sonic corner point. Then, the interaction problem is formulated using the triple-deck model. Lastly, a procedure based on a semi-direct solution of the governing equations using Newton iterations is developed to obtain the numerical solution of the interaction problem.

1. Introduction

The phenomenon of flow separation from a body surface, whether it is smooth or not, has been studied using triple-deck theory by many workers since the end of the 1960s. Most of the works were on supersonic or subsonic flows (see, for example, Stewartson 1970; Neiland 1971; Jenson, Burggraf & Rizzetta 1975 and Ruban 1976, 1978), but little is known about the case when the flow is transonic. This is because the equation describing the inviscid transonic flow, the Kármán–Guderley equation, is nonlinear. Therefore it appears to be impossible to formulate the interaction law in an explicit form which would relate the displacement effect of the boundary layer to the pressure induced in the inviscid part of the flow, as in the subsonic and supersonic cases. Instead of studying the interaction corresponding to a relatively simple interaction law, we have to solve the Kármán–Guderley equation together with the boundary-layer equations in order to cover the transonic nature of the flow field.

There are not many studies which explain the flow properties for transonic speeds as a result of the viscous–inviscid problem near the corner points. The first work on the modern theory of transonic viscous–inviscid interaction was performed by Bodonyi & Kluwick (1977). They considered the free interaction of the boundary layer with inviscid transonic flow for the case when the external flow remains supersonic everywhere. A simple-wave-like solution of the Kármán–Guderley equation was used to relate the streamline slope at the outer edge of the boundary layer to the induced pressure. In this case, a simple interaction law was found between the pressure and the

flow inclination angle, like the Ackeret formula for supersonic flows. It is not surprising that the flow behaviour was found similar to the supersonic interaction case. Later, Bodonyi (1979) investigated the transonic boundary-layer flow near convex corners and again the Prandtl–Meyer relation for the case of the transonic limit ($M_\infty \to 1$) was used as the interaction law, assuming that the velocity is supercritical (greater than the speed of sound) in the inviscid part of the flow. Bodonyi & Kluwick (1982) also considered the supercritical transonic trailing edge of a flat plate when the external flow is slightly supersonic and then Bodonyi & Kluwick (1998) extended this work to a more general case of the transonic viscous–inviscid interaction, but the inviscid flow was still assumed to be slightly supersonic.

The laminar separation at a corner point in transonic flow with a free streamline has been considered by Ruban & Türkyilmaz (2000) who used asymptotic analysis of the Navier–Stokes equations at large values of the Reynolds number. They found that the interaction region is governed by the *inviscid–inviscid interaction* due to the flow field in which the angle of the expansion ramp is assumed to be sufficiently large (an order-one quantity) to cause flow separation at a corner point. It is assumed that the separation region is much longer than the region of interaction which forms in a small vicinity of the corner point. In this case, the high-Reynolds-number limit of the solution of the governing Navier–Stokes equations is represented by the inviscid flow in which the shear layer developing along the separated streamline (also called a free streamline) degenerates into a line of discontinuity of the tangential velocity. However, in the present case, we have investigated the flow field with relatively smaller ramp angle ($O(Re^{-3/10})$) and we look at which values of the ramp angle can cause flow separation in subcritical velocities (less than the speed of sound).

The inviscid transonic flow past a corner appears to be non-unique and may take two different forms. In the first solution, the flow is subsonic everywhere except near the corner point. The second solution describes a smooth transition of the sonic flow into a supersonic one; this flow was considered by Bodonyi & Kluwick (1977, 1982, 1998) and by Bodonyi (1979) for the different flow topologies. We shall develop the theory of incipient separation which is based on the first of the solutions.

In the present work, we shall investigate the incipient separation near a corner point of the body surface which may be observed, for example, when the flap of an aircraft wing is deflected. The purpose of this study is to find the critical deflection angle when an attached flow turns into a separated one, and subcritical velocities have been considered contrary to Bodonyi & Kluwick (1977, 1982, 1998) and Bodonyi (1979). In accordance with the procedure adopted, the analysis of the flow starts with the investigation of the boundary layer near the small vicinity of the corner point using triple-deck analysis. The formulation of the interaction problem needs proper far-field boundary conditions to obtain the desired local solution. These conditions will be acquired from the solution of the Kármán–Guderley equation describing the inviscid part of the flow near the corner points using the hodograph method. Since the corner has two different geometries, the boundary conditions appear to possess two distinct forms. In one case, namely a convex corner, the boundary condition can be written in terms of the Airy Ai function, and the other in terms of the Airy Bi function.

2. Transonic boundary-layer analysis

We shall first analyse the behaviour of the boundary layer in transonic flow near the corner point of ramps, such as in figure 1, and then turn to the inviscid transonic flow analysis for the external flow. We will use Cartesian coordinates $\hat{x}$, $\hat{y}$. The velocity
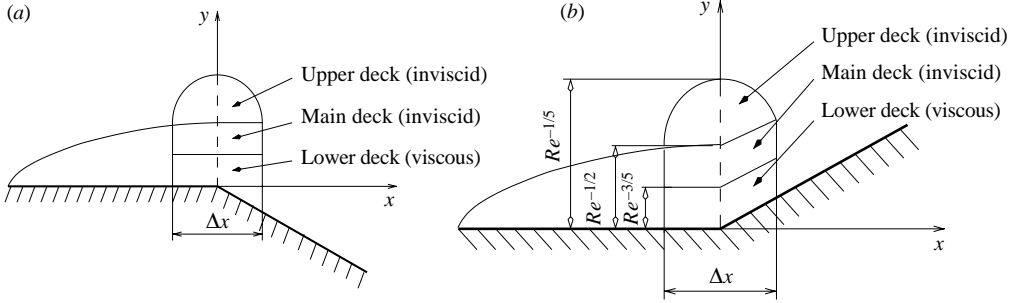
FIGURE 1. Boundary-layer structure with triple deck. (*a*) Convex and (*b*) concave corner.

components in these coordinates will be denoted by $\hat{u}$ and $\hat{v}$. The pressure and gas density will be denoted by $\hat{p}$ and $\hat{\rho}$. In the boundary layer, we also need to consider the enthalpy $\hat{h}$ and dynamic viscosity $\hat{\mu}$. The corresponding non-dimensional variables will be introduced as follows:

$$\hat{u} = \hat{V}_0 u, \quad \hat{v} = \hat{V}_0 v, \quad \hat{p} = \hat{p}_0 + \hat{\rho}_0 \hat{V}_0^2 p,$$
$$\hat{\rho} = \hat{\rho}_0 \rho, \quad \hat{h} = \hat{V}_0^2 h, \quad \hat{\mu} = \hat{\mu}_0 \mu,$$
$$\hat{x} = Lx, \quad \hat{y} = Ly.$$

Recall that suffix '0' is used to denote the values of the corresponding quantities in the inviscid flow just upstream of the interaction region and L is the characteristic length scale. In the following analysis, the Reynolds number

$$Re = \frac{\hat{\rho}_0 \hat{V}_0 L}{\hat{\mu}_0}$$

is assumed large enough, and the asymptotic expansions of the gas dynamic functions in the boundary layer are sought in the form

$$\left.\begin{aligned}
u(x, y; Re) &= U_0(x, Y) + \cdots, \quad v(x, y; Re) = Re^{-1/2} V_0(x, Y) + \cdots, \\
p(x, y; Re) &= P_0(x, Y) + \cdots, \quad \rho(x, y; Re) = \rho_0(x, Y) + \cdots, \\
h(x, y; Re) &= h_0(x, Y) + \cdots, \quad \mu(x, y; Re) = \mu_0(x, Y) + \cdots,
\end{aligned}\right\} \tag{2.1}$$

where, as usual, the coordinate normal to the wall is scaled as

$$y = Re^{-1/2} Y.$$

Substitution of (2.1) into the Navier–Stokes equations gives the following set of equations

$$\rho_0 \left(U_0 \frac{\partial U_0}{\partial x} + V_0 \frac{\partial U_0}{\partial Y} \right) = -\frac{\partial P_0}{\partial x} + \frac{\partial}{\partial Y} \left(\mu_0 \frac{\partial U_0}{\partial Y} \right), \tag{2.2}$$

$$\rho_0 \left(U_0 \frac{\partial h_0}{\partial x} + V_0 \frac{\partial h_0}{\partial Y} \right) = U_0 \frac{\partial P_0}{\partial x} + \frac{1}{Pr} \frac{\partial}{\partial Y} \left(\mu_0 \frac{\partial h_0}{\partial Y} \right) + \mu_0 \left(\frac{\partial U_0}{\partial Y} \right)^2, \tag{2.3}$$

$$\frac{\partial (\rho_0 U_0)}{\partial x} + \frac{\partial (\rho_0 V_0)}{\partial Y} = 0, \tag{2.4}$$

$$\frac{1}{(\gamma - 1)\rho_0} + \frac{\gamma}{\gamma - 1} \frac{P_0}{\rho_0} = h_0. \tag{2.5}$$

Equations (2.2)–(2.5) are in turn the momentum equation projected upon the longitudinal coordinate x, the energy equation with Pr being the Prandtl number, the continuity equation and the state equation. The Prandtl number of unity is used for simplification of the asymptotic analysis. This physically implies that adiabatic flow is effectively present at every point in the boundary layer.

To leading order the pressure in the boundary layer does not change across the boundary layer

$$\frac{\partial P_0}{\partial Y} = 0,$$

which is easily confirmed by substituting (2.1) into the y-component of the momentum equation.

In the inviscid analysis of transonic flows, approaching the corner point on the compression ramp, we know that the pressure has a singularity. This indicates that we have to introduce the triple-deck structure near the corner point. To describe the flow in the triple-deck region, we have to know the asymptotic form of the solution of the Navier–Stokes equations in each of the three layers. To predict this form we perform the so-called inspection analysis (see Appendix A) and the following results have been obtained for the longitudinal extent of the interaction region

$$x \sim Re^{-3/10} \tag{2.6}$$

and for the thickness of the viscous sublayer

$$y \sim Re^{-3/5}. \tag{2.7}$$

Thus, the order of magnitude of inclination angle of the ramp, α, is easily obtained from formulae (2.6) and (2.7) as

$$\alpha \sim \frac{y}{x} \sim Re^{-3/10}.$$

Now we can turn to a rigorous asymptotic analysis of the flow in the three layers of the triple-deck interaction region.

2.1. *Analysis of the viscous sublayer*

Using estimations (2.6) and (2.7), asymptotic analysis of the Navier–Stokes equations may be dealt with using the following limit procedure:

$$X = Re^{3/10}x = O(1), \quad Y_1 = Re^{3/5}y = O(1) \quad \text{as } Re \to \infty.$$

Gas dynamics functions may be represented in this region by the asymptotic expansions

$$\left.\begin{aligned}
u(x, y) &= Re^{-1/10}U_1(X, Y_1) + \cdots, & h(x, y) &= h_1(X, Y_1) + \cdots, \\
v(x, y) &= Re^{-2/5}v_1(X, Y_1) + \cdots, & \rho(x, y) &= \rho_1(X, Y_1) + \cdots, \\
p(x, y) &= Re^{-1/5}P(X, Y_1) + \cdots, & \mu(x, y) &= \mu_1(X, Y_1) + \cdots.
\end{aligned}\right\} \tag{2.8}$$

Substituting (2.8) into the Navier–Stokes equations, we have

$$\frac{\partial U_1}{\partial X} + \frac{\partial V_1}{\partial Y_1} = 0, \tag{2.9}$$

$$\rho_1\left(U_1\frac{\partial U_1}{\partial X} + V_1\frac{\partial U_1}{\partial Y_1}\right) = -\frac{\partial P}{\partial X} + \frac{\partial}{\partial Y_1}\left(\mu_1\frac{\partial U_1}{\partial Y_1}\right), \tag{2.10}$$

$$\frac{\partial P}{\partial Y_1} = 0, \tag{2.11}$$

$$\rho_1\left(U_1\frac{\partial h_1}{\partial X} + V_1\frac{\partial h_1}{\partial Y_1}\right) = \frac{\partial}{\partial Y_1}\left(\frac{\mu_1}{Pr}\frac{\partial h_1}{\partial Y_1}\right). \tag{2.12}$$

The energy equation (2.12) admits a constant-enthalpy solution $h_1 = \text{const}$, which means that the flow in the lower deck may be treated as incompressible. The first boundary condition for equations (2.9)–(2.11) is the no-slip condition, and it should be imposed on the velocity components on the body surface

$$U_1 = V_1 = 0 \quad \text{at } Y_1 = \bar{f}(X), \tag{2.13}$$

where $\bar{f}(X)$ is the shape function of the compression or expansion ramp. Thus, the ramp shape is felt within the lower deck. Equations (2.9) and (2.11) also require an initial condition. It is deduced from matching with the Blasius solution valid in the boundary layer upstream of the interaction region as

$$U_1 = \lambda Y_1 + \cdots \quad \text{as } X \to -\infty. \tag{2.14}$$

Here, λ represents the wall shear in the oncoming boundary layer.

The asymptotic behaviour of the solution of equations (2.9) and (2.10) at the outer edge of the viscous sublayer has been used to find the slope of the streamlines. For this purpose, the stream function ψ may be introduced, based on the continuity equation, such that

$$U_1 = \frac{\partial \psi}{\partial Y_1}, \quad V_1 = -\frac{\partial \psi}{\partial X}.$$

As a result of the asymptotic analysis at the edge of the viscous sublayer, stream function $\psi(X, Y_1)$ may be written as

$$\psi(X, Y_1) = \tfrac{1}{2}\lambda Y_1^2 + A_*(X)Y_1 + \cdots \quad \text{as } Y_1 \to \infty. \tag{2.15}$$

The function $A_*(x)$, apparently, cannot be found from the analysis of the momentum and continuity equations near the outer edge of the viscous sublayer. The entire solution of the problem that describes the flow behaviour between $Y_1 = 0$ and $Y_1 = \infty$ and consideration of the boundary conditions (2.13), (2.14) are necessary. To reveal the physical meaning of function $A_*(X)$, we combine (2.15) with (2.8). As a result, the slope of the streamlines at the outer edge of the viscous sublayer appears to be

$$\theta = \left.\frac{v}{u}\right|_{Y_1\to\infty} = Re^{-3/10}\left[-\frac{1}{\lambda}A_*'(X)\right] + \cdots \tag{2.16}$$

where $A_*(X)$ is called the displacement function.

2.2. *Analysis of the main-deck flow*

Asymptotic analysis of the Navier–Stokes equations in the main part of the boundary layer is based on the following limit procedure:

$$X = Re^{3/10}x = O(1), \quad Y = Re^{1/2}y = O(1) \quad \text{as } Re \to \infty. \tag{2.17}$$

The asymptotic solution of the Navier–Stokes equations in the main part of the boundary layer may be written in the following form:

$$u(x, y) = U_{20}(Y) + Re^{-1/10}U_{21}(X, Y) + \cdots, \quad h(x, y) = h_{20}(Y) + Re^{-1/10}h_{21}(X, Y_1) + \cdots,$$
$$v(x, y) = Re^{-3/10}V_{21}(X, Y) + \cdots, \qquad\qquad \rho(x, y) = \rho_{20} + Re^{-1/10}\rho_{21}(X, Y) + \cdots,$$
$$p(x, y) = Re^{-1/5}P(X, Y) + \cdots, \qquad\qquad \mu(x, y) = \mu_{20} + Re^{-1/10}\mu_{21}(X, Y) + \cdots.$$

Substituting these asymptotic expansions into the Navier–Stokes equations, we have

$$\rho_{20}\left(\frac{\partial U_{21}}{\partial X} + \frac{\partial V_{21}}{\partial Y}\right) + U_{20}\frac{\partial \rho_{21}}{\partial X} + V_{21}\frac{\partial \rho_{20}}{\partial Y} = 0, \tag{2.18}$$

$$\frac{\partial U_{21}}{\partial X} = V_{21}\frac{U'_{20}}{U_{20}}, \tag{2.19}$$

$$\frac{\partial P}{\partial Y} = 0, \tag{2.20}$$

$$U_{20}\frac{\partial h_{21}}{\partial X} + V_{21}\frac{\partial h_{20}}{\partial Y} = 0, \tag{2.21}$$

and from the state equation, h_{20} and h_{21} can be expressed in terms of density and Mach number as

$$h_{20} = \frac{1}{(\gamma - 1)\rho_{20}}, \tag{2.22}$$

$$h_{21} = -\frac{2M_0}{(\gamma - 1)\rho_{20}} - \frac{\rho_{21}}{(\gamma - 1)\rho_{20}^2}. \tag{2.23}$$

Substituting (2.22) and (2.23) into (2.21) gives

$$U_{20}\frac{\partial \rho_{21}}{\partial X} + V_{21}\frac{\partial \rho_{20}}{\partial Y} = 0. \tag{2.24}$$

Taking (2.24) into account, (2.18) simplifies to

$$\frac{\partial U_{21}}{\partial X} + \frac{\partial V_{21}}{\partial Y} = 0. \tag{2.25}$$

Combining (2.25) with (2.19) gives

$$\frac{\partial}{\partial Y}\left(\frac{V_{21}}{U_{20}}\right) = 0 \tag{2.26}$$

which means that the slope of the streamlines, θ, is constant across the main part of the boundary layer.

It follows from the above analysis that the displacement effect of the boundary layer in the three-tiered interaction region is produced entirely by the viscous sublayer. Indeed, at the bottom of the viscous sublayer, the slope angle θ is equal to the slope of the body surface. However, variations in the pressure make the streamlines change their shape and, instead of being parallel to the body surface, they acquire the slope which, at the outer edge of the viscous sublayer, is given in formula (2.16). The slope angle then stays unchanged across the main part of the boundary layer. In the upper deck, it is converted into perturbations of the pressure which penetrate back into the viscous sublayer without any change, in accordance with (2.20). Therefore, in order to close the formulation of the viscous–inviscid interaction problem, the upper deck of the interaction region (see figure 1) remains to be considered.

2.3. *Asymptotic analysis of the upper deck*

In this region, the flow is assumed to be inviscid and irrotational. The asymptotic analysis of the Navier–Stokes equation may be performed based on the following limit procedure:

$$X = Re^{3/10}x = O(1), \quad Y_3 = Re^{1/5}y = O(1) \quad \text{as } Re \to \infty. \tag{2.27}$$

Gas dynamics functions may be represented in the following asymptotic forms:

$$\left.\begin{aligned}
u(x, y) &= 1 + Re^{-1/5}U_{31}(X, Y_3) + \cdots, & v(x, y) &= Re^{-3/10}V_{31}(X, Y_3) + \cdots, \\
\rho(x, y) &= 1 + Re^{-1/5}\rho_{31}(X, Y_3) + \cdots, & p(x, y) &= Re^{-1/5}P_3(X, Y_3) + \cdots.
\end{aligned}\right\} \tag{2.28}$$

Because of the assumptions that the flow is inviscid and irrotational in the upper deck, the Navier–Stokes equations can be reduced to the velocity potential equation. In the potential equation, using Bernoulli's equation, the speed of sound, a, may be deduced to be

$$a^2 = \frac{1}{M_0^2} - Re^{-1/5}(\gamma - 1)M_1 + \cdots,$$

where M_0 is the undisturbed value of the Mach number immediately upstream of the interaction region. We assumed that M_0 has a similar asymptotic form to the longitudinal velocity component as

$$M_0 = 1 + Re^{-1/5}M_1 + \cdots.$$

Hence, the speed of sound a may be reduced to

$$a^2 = 1 - Re^{-1/5}(-2M_1 - (\gamma - 1)U_{31} + \cdots). \tag{2.29}$$

Substitution of the above asymptotic forms (2.28) and (2.29) and collecting the leading-order terms, we have

$$[\mathscr{K}^* - (\gamma + 1)U_{31}]\frac{\partial U_{31}}{\partial X} + \frac{\partial V_{31}}{\partial Y_3} = 0, \tag{2.30}$$

where $\mathscr{K}^*$ is the Kármán–Guderley parameter and $\mathscr{K}^* = -2M_1$ $\mathscr{K}^*$ describes the type of local flow regime; if it is less than zero, the flow is supersonic or greater than zero, the flow becomes subsonic. Moreover, in this region, the pressure distribution can be found in the form of the linearized Bernoulli equation,

$$P_3 = -U_{31}, \tag{2.31}$$

using the inviscid flow theory (see Cole & Cook 1986).

3. Formulation of the interaction problem

In this section, we shall present the formulation of the viscous–inviscid interaction problem for the transonic flow near the corner point of an expansion ramp. Before giving the formulation, we have to find a relation between the displacement function and vertical velocity component at the 'bottom' of the upper-deck region. This relation can be found by performing matching between corresponding layers in the boundary layer.

To perform matching between the viscous sublayer and the main part of the boundary layer, we recall that the slopes of the streamlines in the main part and the outer edge of the viscous sublayer have to coincide with each other in the overlap region.

As a result, we have

$$V_{31}(X, 0) = -\frac{1}{\lambda}A'_*(X). \tag{3.1}$$

Summarizing the results of the above analysis, we note that the flow near to a corner point of a compression or expansion ramp is governed by the interaction between the viscous sublayer and external inviscid transonic flow. The intermediate layer occupying the main part of the boundary layer plays a passive role in the inter-action process. It simply transmits the streamline slope angle generated in the viscous sublayer to the external inviscid flow region, and also transmits the pressure generated in the external flow region to the viscous sublayer without change.

Since the Kármán–Guderley equation governing the inviscid external flow field is nonlinear, we cannot deduce a simple interaction law as in the case of subsonic and supersonic flows or in the work of Bodonyi (1979) corresponding to supercritical flows. However, we can solve the Prandtl equations with the corresponding boundary conditions for the viscous sublayer, and the Kármán–Guderley equations for the inviscid external part of the triple deck separately for a given displacement function to calculate the pressure at each part. After that, the displacement function can be corrected using the Newton method in order to adjust the pressure distributions in the inviscid and viscous parts of the flow.

The flow in the viscous sublayer is governed by the Prandtl boundary-layer equations (2.9)–(2.12). They may be rewritten as

$$\left. \begin{aligned} \rho_1\left(U_1\frac{\partial U_1}{\partial X} + V_1\frac{\partial U_1}{\partial Y_1}\right) &= -\frac{\partial P}{\partial X} + \mu_1\frac{\partial^2 U_1}{\partial Y_1^2}, \\ \frac{\partial U_1}{\partial X} + \frac{\partial V_1}{\partial Y_1} &= 0, \end{aligned} \right\} \tag{3.2}$$

which have to be solved with the boundary conditions (2.13), (2.14) and (2.15),

$$\left. \begin{aligned} U_1 &= \lambda Y_1 + \cdots && \text{as } X \to -\infty, \\ U_1 &= \lambda Y_1 + A_*(X) + \cdots && \text{as } Y_1 \to \infty, \\ U_1 &= V_1 = 0 && \text{at } Y_1 = \bar{f}(X). \end{aligned} \right\} \tag{3.3}$$

The flow in the inviscid external part of the triple-deck structure is governed by the Kármán–Guderley equation (2.30) and the irrotationality equation. They are written as

$$\left. \begin{aligned} [\mathscr{K}^* - (\gamma + 1)U_{31}]\frac{\partial U_{31}}{\partial X} + \frac{\partial V_{31}}{\partial Y_3} &= 0, \\ \frac{\partial U_{31}}{\partial Y_3} - \frac{\partial V_{31}}{\partial X} &= 0, \end{aligned} \right\} \tag{3.4}$$

which have to be solved subject to the boundary conditions (2.31), (3.1) and they may be rewritten as

$$\left. \begin{aligned} P_3 &= -U_{31}|_{Y_3=0}, \\ V_{31}|_{Y_3=0} &= -\frac{1}{\lambda}A'_*(X) + \cdots. \end{aligned} \right\} \tag{3.5}$$

Note that $P = P_3$ on $Y_3 = 0$.

We also have to use the far-field boundary conditions which have been obtained from the analysis of the inviscid transonic flows near to the corner point in the hodograph plane.

It is convenient to scale out the constants λ, ρ_1, μ_1 from these equations (3.2), (3.4) and the boundary conditions (3.3), (3.5) by using the affine transformations

$$U_1 = \mu_1^{1/7}\rho_1^{-9/14}\lambda^{-1/7}U, \qquad\qquad V_1 = \mu_1^{4/7}\rho_1^{-15/14}\lambda^{-4/7}\left(V + U\frac{\mathrm{d}f}{\mathrm{d}x}\right),$$

$$P_1 = \mu_1^{2/7}\rho_1^{-2/7}\lambda^{-2/7}P, \qquad\qquad Y_1 = \mu_1^{1/7}\rho_1^{-9/14}\lambda^{-8/7}(y + f(x)),$$

$$U_{31} = \mu_1^{2/7}\rho_1^{-2/7}\lambda^{-2/7}\bar{U}, \qquad\qquad V_{31} = \mu_1^{3/7}\rho_1^{-3/7}\lambda^{-3/7}\bar{V},$$

$$X = \mu_1^{-2/7}\rho_1^{-3/14}\lambda^{-5/7}x, \qquad\qquad Y_3 = \mu_1^{-4/7}\rho_1^{-1/14}\lambda^{-3/7}\bar{y},$$

$$A_* = \mu_1^{1/7}\rho_1^{-9/14}\lambda^{-1/7}(A - f(x)), \qquad \mathscr{K}^* = \mu_1^{2/7}\rho_1^{-2/7}\lambda^{-2/7}\mathscr{K},$$

$$\bar{\theta}_0 = \mu_1^{3/7}\rho_1^{-3/7}\lambda^{-3/7}\theta_0, \qquad\qquad \bar{f}(X) = \mu_1^{1/7}\rho_1^{-9/14}\lambda^{-8/7}f(x).$$

As a result, the transonic viscous–inviscid interaction problem takes the following canonical form. For the viscous sublayer, we have

$$U\frac{\partial U}{\partial x} + V\frac{\partial U}{\partial y} = -\frac{\partial P}{\partial x} + \frac{\partial^2 U}{\partial y^2}, \tag{3.6a}$$

$$\frac{\partial U}{\partial x} + \frac{\partial V}{\partial y} = 0, \tag{3.6b}$$

which should be solved with the boundary conditions

$$U = y + \cdots \qquad \text{as } x \to -\infty, \tag{3.7a}$$

$$U = y + A(x) + \cdots \qquad \text{as } y \to \infty, \tag{3.7b}$$

$$U = V = 0 \qquad \text{at } y = 0. \tag{3.7c}$$

For the inviscid external flow

$$\left.\begin{aligned} [\mathscr{K} - (\gamma + 1)\bar{U}]\frac{\partial\bar{U}}{\partial x} + \frac{\partial\bar{V}}{\partial\bar{y}} &= 0, \\ \frac{\partial\bar{U}}{\partial\bar{y}} - \frac{\partial\bar{V}}{\partial x} &= 0, \end{aligned}\right\} \tag{3.8}$$

and corresponding boundary conditions at $\bar{y} = 0$ are

$$\left.\begin{aligned} P &= -\bar{U}, \\ \bar{V} &= -A'(x) + f'(x) + \cdots. \end{aligned}\right\} \tag{3.9}$$

We also need to formulate the far-field boundary conditions of the external inviscid flow. For this purpose, we introduce so called hodograph analysis. In this approach, the Kármán–Guderley equation and irrotationality equation may be written in the following form:

$$\left.\begin{aligned} w\frac{\partial w}{\partial x} - \frac{\partial\vartheta}{\partial\bar{y}} &= 0, \\ \frac{\partial w}{\partial\bar{y}} - \frac{\partial\vartheta}{\partial x} &= 0, \end{aligned}\right\} \tag{3.10}$$

where $w = (\gamma + 1)\bar{U} - \mathscr{K}$, $\vartheta = (\gamma + 1)\bar{V}$.

The flow field is bounded by two flat plates, one is horizontal and placed on the negative x-axis and the other is deflected at an angle $\alpha = \varepsilon\bar{\theta}_0$ with $\varepsilon = O(Re^{-3/10}) \ll 1$
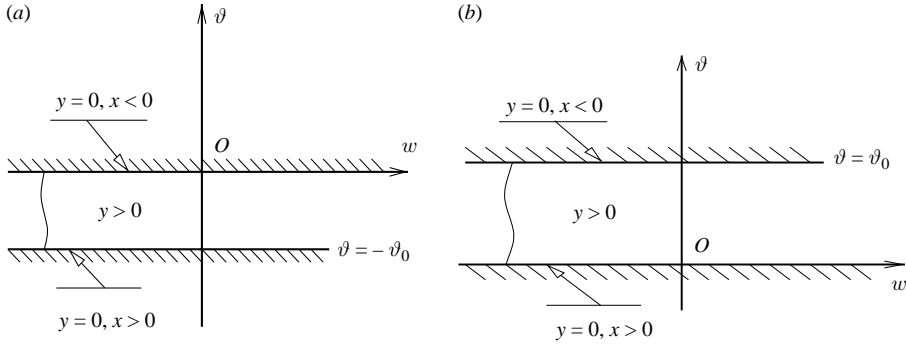
FIGURE 2. Boundary conditions in the hodograph plane. (*a*) Convex and (*b*) concave corner.

and $\bar{\theta}_0$ is an order-one quantity, as shown in figure 1. The corresponding boundary conditions for this flow may be written as

$$\vartheta|_{\bar{y}=0} = \begin{cases} 0 & \text{for } x < 0, \\ \vartheta_0 & \text{for } x > 0, \end{cases} \tag{3.11}$$

where $\vartheta_0 = (\gamma + 1)\bar{\theta}_0 > 0$.

The hodograph method deals with the inverted form of (3.10). The resulting equations, known as the hodograph equations, have the velocity components w, ϑ as independent variables, and the coordinates x, $\bar{y}$, as the sought functions. These equations are easier to deal with than (3.10) since they are linear. Hence, the governing equations (3.10) may be written in the hodograph variables as follows

$$w\frac{\partial \bar{y}}{\partial \vartheta} - \frac{\partial x}{\partial w} = 0, \tag{3.12a}$$

$$\frac{\partial \bar{y}}{\partial w} - \frac{\partial x}{\partial \vartheta} = 0. \tag{3.12b}$$

Eliminating x from this system of equations yields the well-known Tricomi equation

$$w\frac{\partial^2 \bar{y}}{\partial \vartheta^2} - \frac{\partial^2 \bar{y}}{\partial w^2} = 0. \tag{3.13}$$

This is a variable coefficient partial differential equation which changes its type as w changes its sign. If $w < 0$ the equation is elliptic, if $w > 0$ the equation is hyperbolic. The line $w = 0$, the ϑ-axis in the hodograph plane, is a sonic line.

The boundary conditions in the physical plane can be converted in the hodograph plane as follows for the case of a concave corner (compression ramp)†. The first boundary is represented by the flat plate upstream of the corner. Here $\vartheta = 0$ and $y = 0$ (see figure 2b). Downstream of the corner $\vartheta = \vartheta_0$ on the body surface, and we set $\bar{y} = 0$ on this surface since the vertical velocity component is assumed to be small in the transonic small perturbation theory. We further note that $\bar{y} > 0$ in the flow field. The solution of Tricomi equation (3.13) using separation of variables, can be represented as

$$\bar{y}(w, \vartheta) = W(w)\Theta(\vartheta). \tag{3.14}$$

---

† When it is convex (see figure 2a), the same analysis can be used to obtain the solution of the Kármán–Guderley equation.

Hence, the solution of the Tricomi equation corresponding to the present boundary conditions can be written as

$$\bar{y} = C \sin(\mu\vartheta)\mathrm{Ai}\left(-\mu^{2/3}w\right), \tag{3.15}$$

where C is the constant of integration and has been chosen to be unity in the rest of the paper. Since y is positive, Ai remains positive when w satisfies the restriction†

$$\mu^{2/3}w \leqslant |a_1|,$$

where $a_1 = -2.33810$ is the first zero of the function $\mathrm{Ai}(x)$ (see Abramowitz & Stegun 1965). As a result, w becomes less than zero and the velocity field becomes subcritical.

So far we have found the relationship between y and the velocity components. Now we substitute (3.15) into (3.12*b*). This yields

$$x = \frac{1}{\mu^{1/3}} \cos(\mu\vartheta)\,\mathrm{Ai}'\left(-\mu^{2/3}w\right) + \chi(w). \tag{3.16}$$

To find the function $\chi(w)$, (3.12*a*) is used, taking into account that $\mathrm{Ai}''(s) = s\,\mathrm{Ai}(s)$, we have

$$\chi'(w) = 0.$$

Thus, $\chi(w)$ is constant and represents a shift along the x-axis, or the location of the corner point with respect to the x-axis. Hence, without lost of generality, it can be set to zero. Thus, (3.16) may be written as

$$x = \frac{1}{\mu^{1/3}} \cos(\mu\vartheta)\,\mathrm{Ai}'\left(-\mu^{2/3}w\right). \tag{3.17}$$

The equations (3.15) and (3.17) together suggest that the horizontal velocity has to satisfy the condition

$$\mu^{2/3}w \leqslant |a_1'|,$$

where $a_1' = -1.01879$ (see Abramowitz & Stegun 1965).

To find the asymptotic behaviour of the solution (3.15) far from the corner, asymptotic forms of the Airy Ai and Ai′ functions (see Abramowitz & Stegun 1965) have been used in (3.15) and in (3.17). Hence, we have the leading-order approximation of the far-field boundary conditions in the closed form as

$$\left.\begin{aligned} x &= -\frac{\cos(\mu\vartheta)}{2\sqrt{\pi}\sqrt[6]{\mu}}(-w)^{1/4}\exp\left(-2/3\mu(-w)^{3/2}\right),\\[2mm] \bar{y} &= \frac{\sin(\mu\vartheta)}{2\sqrt{\pi}\mu^{1/6}}(-w)^{-1/4}\exp\left(-2/3\mu(-w)^{3/2}\right), \end{aligned}\right\} \tag{3.18}$$

where $w = (\gamma + 1)\bar{U} - \mathcal{K}$ and $\vartheta = (\gamma + 1)\bar{V}$.

The same analysis can be repeated for the case of the convex corner problem considering the boundary conditions (see figure 2*a*); $\vartheta = 0$ and $\bar{y} = 0$, downstream of the corner $\vartheta = -\vartheta_0$ on the body surface, $\bar{y} = 0$ on this surface. In this case, the solution of the Kármán–Guderley equation may be found in terms of Airy Bi function and its derivative as

$$\left.\begin{aligned} x &= -\frac{1}{\mu^{1/3}} \cos(\mu\vartheta)\,\mathrm{Bi}'\left(-\mu^{2/3}w\right),\\[2mm] \bar{y} &= -\sin(\mu\vartheta)\,\mathrm{Bi}\left(-\mu^{2/3}w\right). \end{aligned}\right\} \tag{3.19}$$

† For other intervals, Ai becomes oscillating and hence violates the condition $\bar{y} >$ zero.

Making use of the asymptotic properties of the Airy Bi and Bi′ functions (see, Abramowitz & Stegun 1965), the leading-order approximation of (3.19) may be written as

$$
\left.
\begin{aligned}
x &= -\frac{\cos(\mu\vartheta)}{\mu^{1/6}\sqrt{\pi}}(-w)^{1/4}\exp\big(2/3\mu(-w)^{3/2}\big),\\
\bar{y} &= -\frac{\sin(\mu\vartheta)}{\mu^{1/6}\sqrt{\pi}}(-w)^{-1/4}\exp\big(2/3\mu(-w)^{3/2}\big),
\end{aligned}
\right\}
\tag{3.20}
$$

Hence, we have the corresponding representation of the far-field boundary conditions for the convex-corner problem.

Summarizing this analysis, we can conclude that the Kármán–Guderley equation admits a solution in the form of Airy functions which may be used to formulate the far-field boundary conditions for the upper-deck of the triple-deck flow near the corner point in order to preserve the transonic nature of the local flow field in the cases of the expansion or compression ramp.

4. Numerical solution of the interaction problem

In the previous section, the interaction process of the transonic flow field near to the corner point of the expansion/compression ramp has been formulated. In this section, we will give a description of the numerical method to solve the interaction problem.

It is known that the pressure does not changes across the boundary layer. Hence the pressure distribution on the body surface in the boundary layer has to coincide with the pressure distribution generated by the external flow at the bottom of the upper deck. This can happen only if the distributions of the displacement function $A(x)$ are properly chosen. The pressure at the bottom of the inviscid flow $P_{inv}(x)$ may be calculated for the given displacement function $A(x)$ using (3.8)–(3.18). To calculate the pressure in the viscous flow $P_{vis}(x)$, we have to use (3.6)–(3.7). We shall write these functions in vectorial form and require that

$$
\boldsymbol{P}_{inv}(\boldsymbol{A}) = \boldsymbol{P}_{vis}(\boldsymbol{A}).
\tag{4.1}
$$

Here $\boldsymbol{P}_{inv}$, $\boldsymbol{P}_{vis}$ and $\boldsymbol{A}$ are vector quantities and their components, namely, P_i^{inv} and P_i^{vis} are the pressures calculated in the inviscid part and viscous sublayer of the triple deck at the grid points $x = x_i$ for $i = 0, \ldots, I_m$, and A_i are the values of the displacement function at these points, respectively. To solve (4.1) the Newton–Raphson linearization has been used. With $\boldsymbol{A}_{old}$ denoting an approximation to A given as an initial guess or found from the previous iteration, an improved approximation,

$$
\boldsymbol{A} = \boldsymbol{A}_{old} + \Delta\boldsymbol{A},
\tag{4.2}
$$

may be found by substituting (4.2) into (4.1) and making the use of the Taylor expansions. This gives the following equation for the correction vector $\Delta\boldsymbol{A}$.

$$
\left[\frac{\partial\boldsymbol{P}_{inv}}{\partial\boldsymbol{A}} - \frac{\partial\boldsymbol{P}_{vis}}{\partial\boldsymbol{A}}\right]\Delta\boldsymbol{A} = \boldsymbol{P}_{vis}(\boldsymbol{A}_{old}) - \boldsymbol{P}_{inv}(\boldsymbol{A}_{old}).
\tag{4.3}
$$

This is a linear algebraic set of equations written in vector form. The coefficient matrix involves derivatives of the pressures with respect to displacement thickness and they are not known in advance.

To start the calculation, an initial guess has been assigned to the displacement vector A. With this initial guess, $\boldsymbol{P}_{inv}$ and $\boldsymbol{P}_{vis}$ have been calculated and then an

increment ϵ (taken as 10^{-3} in the numerical calculations) has been given to the A_i component of the displacement vector A such that the new displacement vector has become

$$A^{(i)} = \left[A_0, A_1, \ldots, A_i + \epsilon, \ldots, A_{I_m}\right]^{\mathrm{T}}.$$

In each ith step of the procedure, using the displacement vector $A^{(i)}$, $P_{inv}^{(i)}$ and $P_{vis}^{(i)}$ have been calculated from the solvers of the external inviscid flow and viscous sublayer equations.

Consequently, the coefficients of the matrix equation (4.3) have been known, so this equation can be solved using a suitable solver. The solution of (4.3) gives the correction vector ΔA and using (4.2) we can find a new displacement vector A. Using these results, the displacement vector A can be updated calculating the pressure distributions again from the solvers of external inviscid flow and viscous sublayer equations, P_{inv} and P_{vis}, respectively. This procedure has been repeated as many times as it has been required for the accuracy criterion

$$M = \text{maximum value of } \{|P_{inv} - P_{vis}|\} < \text{tolerance}$$

to be met (the tolerance has been taken as 10^{-6} in the calculations).

4.1. *Numerical method for the external flow*

We shall now give a description of the numerical scheme used for the external inviscid transonic flow. For this purpose, it is convenient to write (3.8) in terms of the velocity potential

$$[\mathscr{K} - (\gamma + 1)\phi_x]\phi_{xx} + \phi_{\bar{y}\bar{y}} = 0. \tag{4.4}$$

The corresponding boundary conditions are written as

$$P = -\phi_x + \cdots \qquad \text{at } \bar{y} = 0, \tag{4.5}$$

$$\phi_y = A'(x) + f'(x) + \cdots \quad \text{at } \bar{y} = 0, \tag{4.6}$$

which should be supplemented with the far-field boundary conditions (3.18). The computation of the expansion/compression ramp flow has been performed in this study for a slightly smoothed body shape

$$f(x) = \tfrac{1}{2}\theta_0\left[x + (x^2 + r^2)^{1/2}\right],$$

which was used in the boundary condition (4.6). Here, θ_0 is the scaled inclination angle of the expansion/compression ramp and r is the smoothing parameter which slightly rounds the corner; it was typically taken to be $r = 0.5$.

The numerical calculations have been performed in a rectangular domain $ABCD$ shown in figure 3. A uniform grid has been adopted in both the x and $\bar{y}$ directions. The grid function for the velocity potential ϕ has been introduced for the node points $(x_i, \bar{y}_j)$ according to the rule

$$\phi_{i,j} = \phi(x_i, \bar{y}_j) \quad \text{for all } \begin{cases} i = 0, \ldots, I_m, \\ j = 0, \ldots, J_m. \end{cases}$$

To start the numerical calculations, we have to specify an initial distribution of the grid function, ϕ along the rectangle $ABCD$. For this purpose, the far-field behaviour (3.18) was extended to the entire computational domain. This required us to solve (3.18), for which purpose the Newton method was used.

The solution of (4.4) inside the computational domain was then constructed by means of successive iterations. The procedure was based on the conventional line
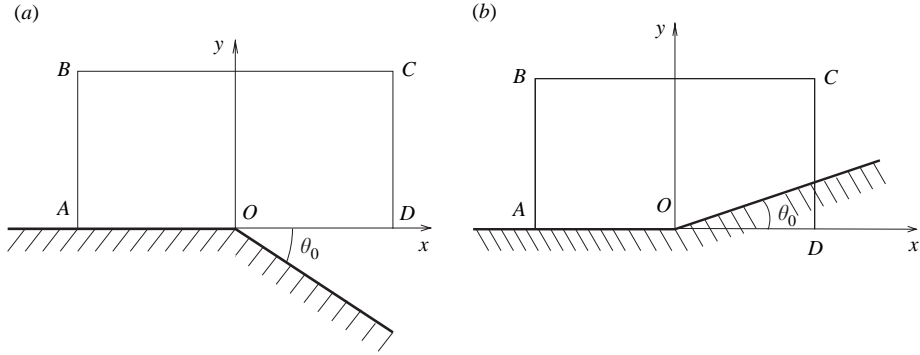
İ. *Türkyilmaz*

FIGURE 3. Computational domain.

relaxation. Starting with the second mesh line ($i = 2$), we marched downstream through the computational domain until the line ($i = I_m - 1$), and on each line ($i = 2, \ldots, I_m - 1$) a tridiagonal set of algebraic equations

$$a_j \phi_{i,j+1} + b_j \phi_{i,j} + c_j \phi_{i,j-1} + d_j = 0 \qquad (j = 1, \ldots, J_m - 1), \qquad (4.7)$$

was formulated by the finite-difference approximation of the Kármán–Guderley equation (4.4). Since (4.4) is a mixed-type partial differential equation, and a choice of the computational stencil at each grid point was decided based on the sign of $\mathcal{K} - (\phi_x)_{i,j}$ (for details see Appendix B.1).

Once the potential ϕ has been found, we can calculate the pressure at the bottom of the inviscid region using the first boundary condition in (3.9). This yields the 'inviscid' pressure vector

$$\boldsymbol{P}_{inv} = \{P_0^{inv}, P_1^{inv}, \ldots, P_{I_m}^{inv}\}. \qquad (4.8)$$

where $P_i^{inv} = P(x_i)$ for $i = 0, \ldots, I_m$.

4.2. *Numerical solution of the boundary-layer equations*

In this section, we shall give a description of the numerical method used for solving the boundary-layer equations (3.6) with boundary conditions (3.7). In this method, the formulation is based on the shear

$$\omega = \frac{\partial U}{\partial y}. \qquad (4.9)$$

Differentiating (3.6a) with respect to y and using (3.6b), we eliminate the pressure leading to the following equation for ω

$$U \frac{\partial \omega}{\partial x} + V \frac{\partial \omega}{\partial y} = \frac{\partial^2 \omega}{\partial y^2}. \qquad (4.10)$$

Two boundary conditions for this equation

$$\omega = 1 \quad \text{at} \quad x = -\infty, \qquad (4.11)$$
$$\omega = 1 \quad \text{at} \quad y = \infty, \qquad (4.12)$$

immediately follow from (3.7a) and (3.7b). The third boundary condition may be deduced by setting $y = 0$ in the momentum equation of (3.6) and using the no-slip

condition of (3.7). This yields

$$\frac{\partial \omega}{\partial y} = \frac{\partial P}{\partial y} \quad \text{at } y = 0. \tag{4.13}$$

With known ω, the longitudinal velocity component may be determined by integrating (4.9) with the first condition of the no-slip conditions of (3.7) used as an initial condition. We have

$$U = \int_0^y \omega \, dy_1. \tag{4.14}$$

Introducing the stream function Ψ, we have

$$U = \frac{\partial \Psi}{\partial y}, \quad V = -\frac{\partial \Psi}{\partial x},$$

which allows the vertical velocity component V to be calculated.

Finally, (4.10) with the boundary conditions (4.11), (4.12) and (4.13) closes the formulation of the boundary-layer equation in terms of the shear.

To construct a numerical solution of (4.10) subject to boundary conditions (4.11), (4.12), a finite-difference technique has been used which may be described as follows. We introduce a mesh (x_i, y_j) $(i = 0, 1, \ldots, I_m, j = 0, 1, \ldots, J_m)$ and denote the values of ω at the node points (x_i, y_j) via $\omega_{i,j}$; considered together they constitute the grid function $\{\omega_{i,j}\}$. Since pressure is independent of y, it may be represented by the grid function $\{P_i\}$ whose elements are defined as $P_i = P(x_i)$.

The numerical procedure is based on the conventional line relaxation. Starting with the second mesh line $(i = 1)$, we marched downstream through the computational domain, and on each of the lines $(i = 1, \ldots, I_m - 1)$, a tridiagonal set of algebraic equations

$$a_j \omega_{i,j+1} + b_j \omega_{i,j} + c_j \omega_{i,j-1} + d_j = 0 \qquad (j = 1, \ldots, J_m - 1), \tag{4.15}$$

was formulated by the following finite-difference approximation of (4.10). Since (4.10) is a parabolic-type equation, the choice of the computational stencil at each grid point was decided based on the sign of $U_{i,j}$, the in the coefficients (for details see Appendix B.2). To calculate $U_{i,j}$, the trapezium rule has been used for the integral on the right-hand side of (4.14).

With the known shear $\omega_{i,j}$, the pressure distribution may be calculated with integrating (4.13) as

$$P_i = P(x_i) = \int_{x_{min}}^{x_i} \frac{\partial \omega}{\partial y} \, dx \quad \text{at } y = 0.$$

Writing this formula in finite-difference form, we find that for $i = 1, 2, \ldots, I_m$

$$P_i = P_0 + \frac{\Delta x}{2\Delta y} \sum_{k=1}^{i} [-3(\omega_{k,0} + \omega_{k-1,0}) + 4(\omega_{k,1} + \omega_{k-1,1}) - (\omega_{k,2} + \omega_{k-1,2})].$$

Here, P_0 is evaluated using the far-field solution (3.18). This procedure gives the 'viscous pressure' vector as

$$\boldsymbol{P}_{vis} = \{P_0^{vis}, P_1^{vis}, \ldots, P_{I_m}^{vis}\}, \tag{4.16}$$

where $P_i^{inv} = P_i$ for $i = 0, \ldots, I_m$.

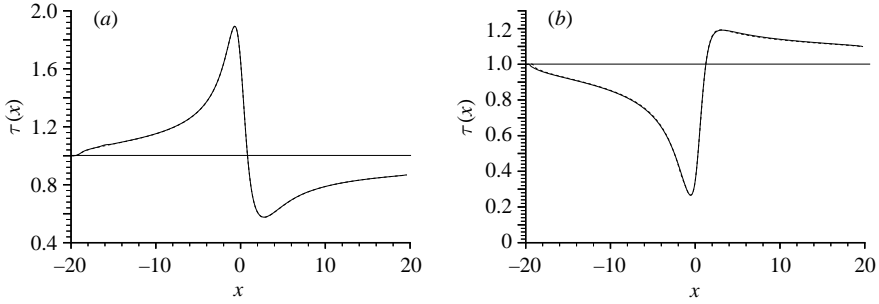FIGURE 4. Skin friction distribution for $\mathcal{K}=1$ and $\theta_0=5$; solid line for mesh 200×100 and dotted line mesh 100×100. (a) Convex and (b) Concave corner.
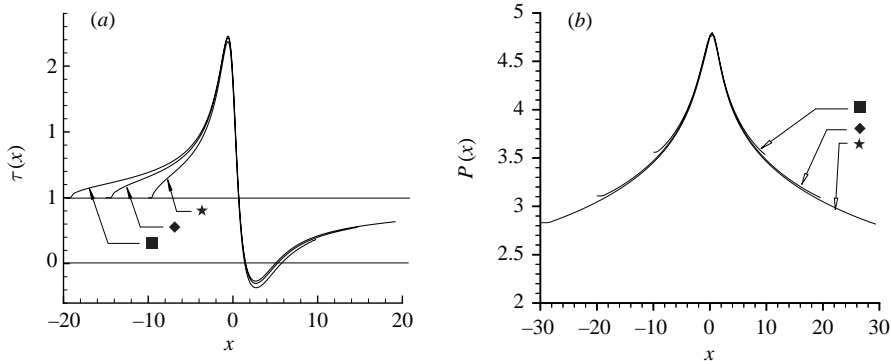

FIGURE 5. Numerical results for different intervals; $\star$, $[-30, 30]$; $\blacklozenge$, $[-20, 20]$; $\blacksquare$, $[-10, 10]$. (a) Skin friction distribution for $\mathcal{K}=1$ and $\theta_0=9$ in the case of a convex corner. (b) Pressure distribution for $\mathcal{K}=1$ and $\theta_0=5.0$ in the case of a concave corner.

5. Results and discussion

The numerical procedure described in the previous section was applied to the expansion and compression ramp problem in the following way. We started with a relatively small value of the scaled ramp angle, namely $\theta_0=1.0$, using the unperturbed flow field $\omega_{i,j}=1$, $V_{i,j}=0$ and $U_{i,j}=y_j$ for the initialization of the unknowns. Keeping the Kármán–Guderley parameter $\mathcal{K}$ fixed, angle θ_0 was increased progressively, and for each new θ_0, the converged solution corresponding to a smaller θ_0 was used as an initial guess to start the iterations. This procedure was repeated for different values of $\mathcal{K}$. Typically, three or four iteration were required for the convergence of iterations in (4.3) to be reached.

Calculations were repeated for different mesh sizes and interval $[-x_\infty, x_\infty]$, such as in figures 4 and 5 to study the mesh and interval dependency of the numerical results. As figure 5 shows the results of the calculations obtained on the intervals, $x \in [-20, 20]$ and $x \in [-30, 30]$ appear to be almost indistinguishable within the interval $x \in [-5, 5]$ (keep in mind that we are interested in the local solution of the flow field) as the length of the intervals increases. The results of the present numerical analysis are presented for the different values of $\mathcal{K}$ and θ_0 in figures 9 to 13.

In the expansion-ramp problem, the wall pressure distribution for different values of $\mathcal{K}$ shown in figure 8 implies that the velocity increases towards the corner point and then decreases again. For sufficiently large values of θ_0, the flow field has a small
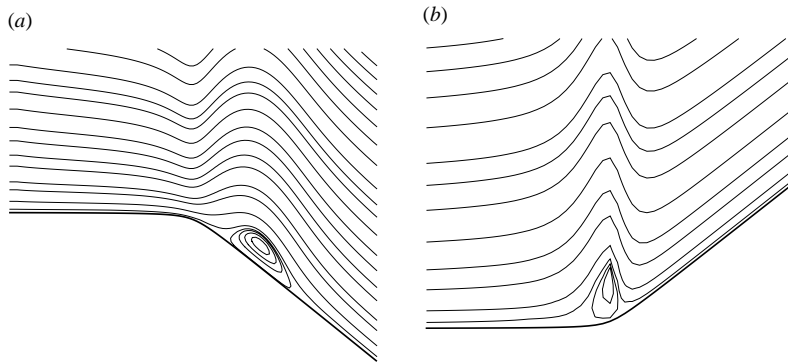
FIGURE 6. Streamlines when the angle is $\theta_0 = 8.0$ for $\mathcal{K} = 0$. The inclination angle is exaggerated for the sake of clarity.
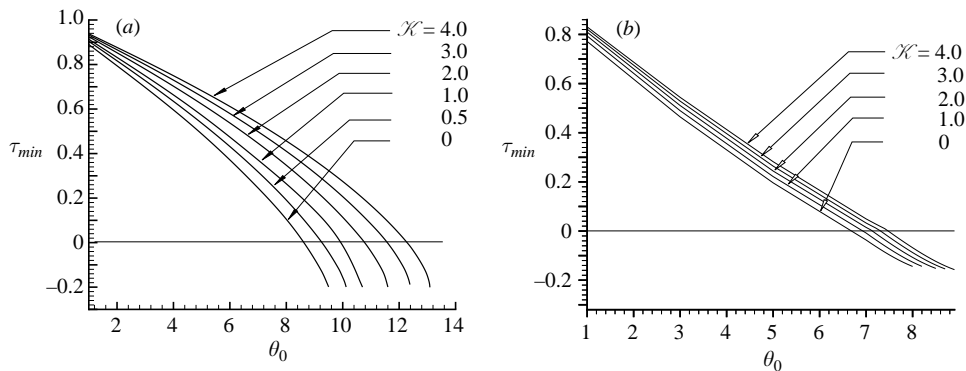

FIGURE 7. Dependence of the minimum value of skin friction for different values of Kármán–Guderley parameter $\mathcal{K}$.

supersonic region. When the value of $\mathcal{K}$ decreases, the supersonic zone appears to be larger for the smaller values of the ramp angle. Meanwhile, when values of $\mathcal{K}$ are greater than 0.5, despite the peak in the velocity, subsonic flow properties become dominant in the flow field and the supersonic zone disappears near the corner point. We see that as a result of the flow acceleration near the corner, the skin friction $\tau(x) = (\partial u / \partial y)|_{y=0}$ increases upstream of the corner more rapidly as the value of θ_0 increases (see figure 10). The maximum skin friction is reached near the corner point and then downstream τ first drops below the unperturbed value $\tau = 1$, and after that, despite a continuing pressure increase, it starts to grow. For sufficiently large value of θ_0, a region of recirculating flow has been formed in the boundary layer downstream of the corner. The fluid motion within this region remains slow and is characterized by small negative values of the skin friction and moderate adverse pressure gradient. Thus, the fluid deceleration beyond the corner is more intense than its acceleration ahead of the corner point. Beginning with a critical value of the parameter θ_0, this deceleration results in the flow separation. The formation of the separation in the transonic flow with subsequent 're-attachment' some distance downstream may be observed in figure 10. The separation grows in size as θ_0 increases. In the present case, the entire region of recirculating flow is located behind the corner. The streamline pattern for $\mathcal{K} = 0$ and $\theta_0 = 9.4$ is shown in figure 6(a).
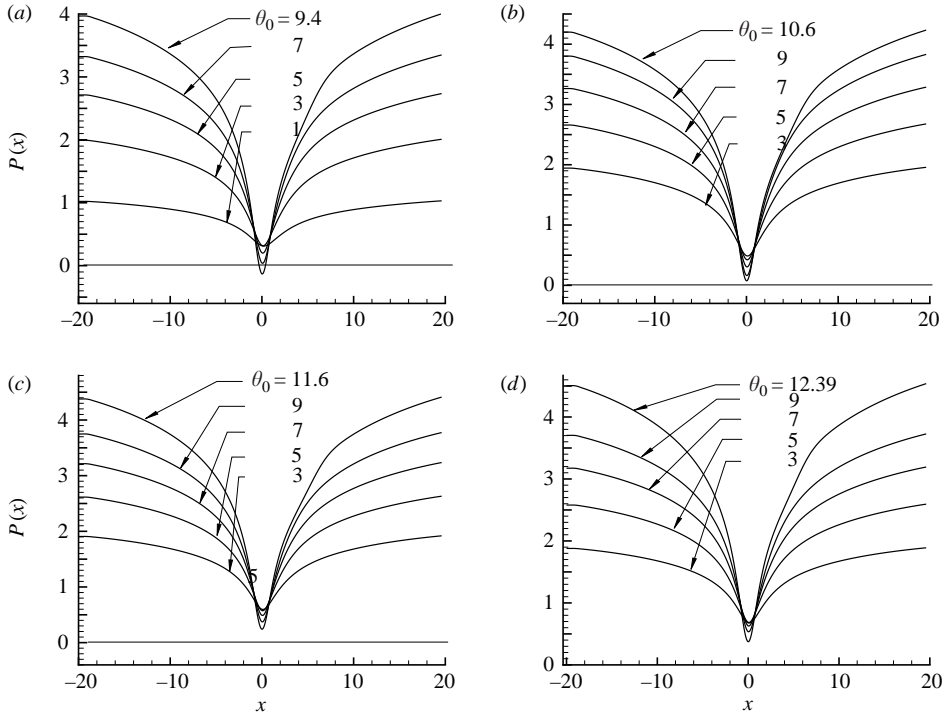
FIGURE 8. Pressure distribution is presented for different values of the Kármán–Guderley parameter $\mathcal{K}$ for the case of an expansion ramp. In each figure, numerical results also are presented for several different ramp angles. (*a*) $P(x)$ for $\mathcal{K} = 0$, (*b*) 1, (*c*) 2, (*d*) 3.
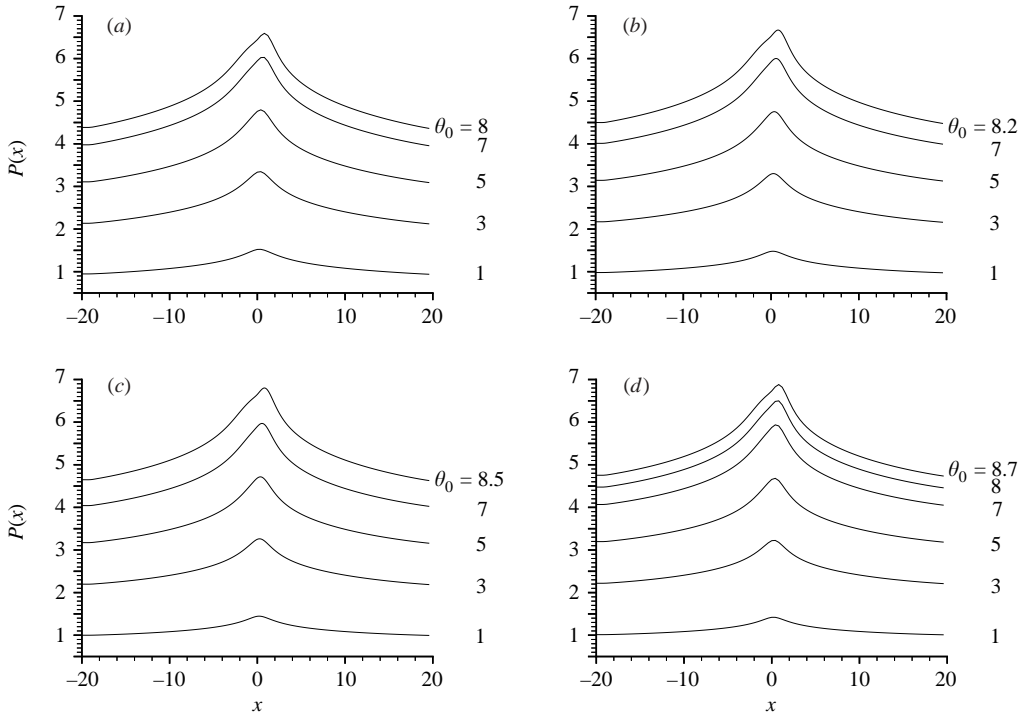

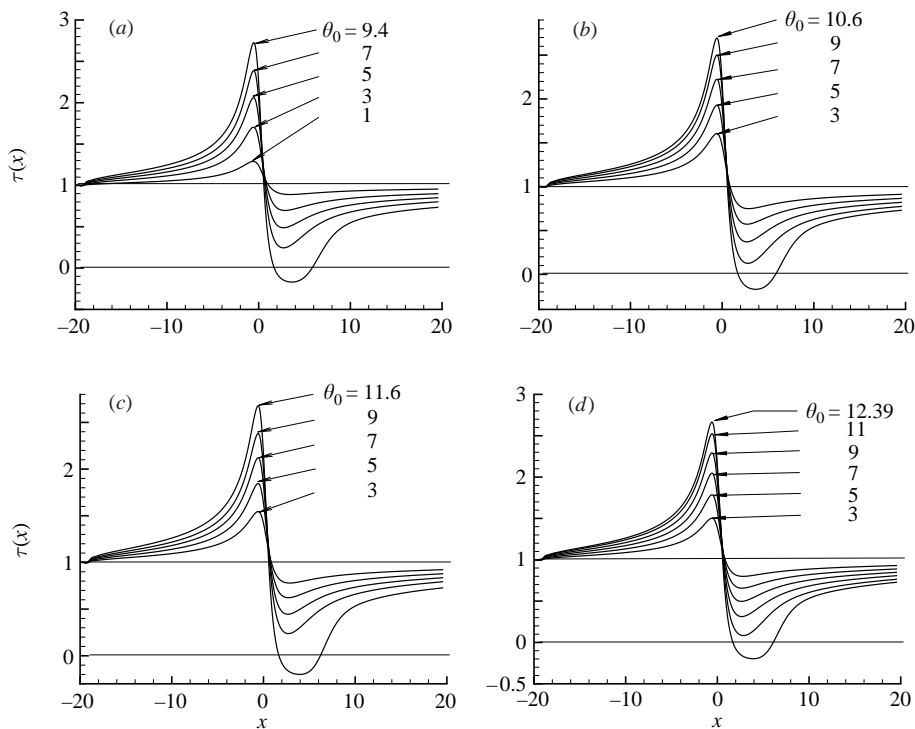FIGURE 9. As for figure 8, but for a compression ramp.

FIGURE 10. Skin friction distribution is presented for different values of the Kármán–Guderley parameter $\mathcal{K}$ for the case of an expansion ramp. In each figure, numerical results also are presented several different for ramp angles. (a) $\tau(x)$ for $\mathcal{K} = 0$, (b) 1, (c) 2, (d) 3.

The incipient separation occurs in the expansion ramp when θ_0 has the value of 8.2 for $\mathcal{K} = 0$, as shown in figure 6(a). Moreover, as $\mathcal{K}$ increases the incipient separation appears for the greater values of ramp angle θ_0. Figures 10(a) and 12(a) show the corresponding distributions of the skin friction and the displacement function for $\mathcal{K} = 0$.

In the case of a compression ramp, the wall pressure distribution for different values of $\mathcal{K}$ shown in figure 9 imply that the velocity in the external inviscid flow decreases towards the corner point and then increases again, but it cannot produce any small supersonic region as in the case of a convex corner.

We see that as a result of the flow deceleration near the corner, the skin friction decreases upstream of the corner more rapidly as the value of θ_0 increases (see figure 11). The minimum skin friction is reached near the corner point and then downstream τ first increases above the unperturbed value $\tau = 1$, and after that, despite a continuing pressure decrease, it starts to decay. For sufficiently large values of θ_0, a region of recirculating flow is formed in the boundary layer near the corner. The fluid motion within this region remains slow and is characterized by small negative values of the skin friction and moderate adverse pressure gradient. Thus, the fluid acceleration beyond the corner is more intense than its deceleration ahead of a corner point. Beginning with a certain value of the parameter θ_0, this deceleration results in the flow separation. The separation grows in size as θ_0 increases. Note that in the present
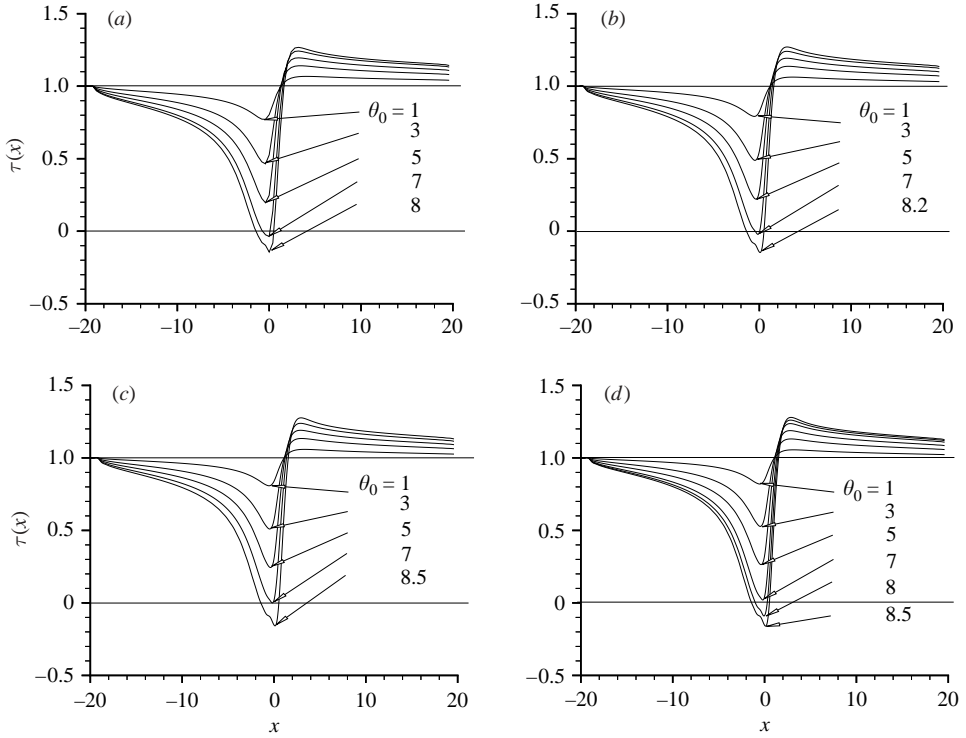
İ. Türkyilmaz

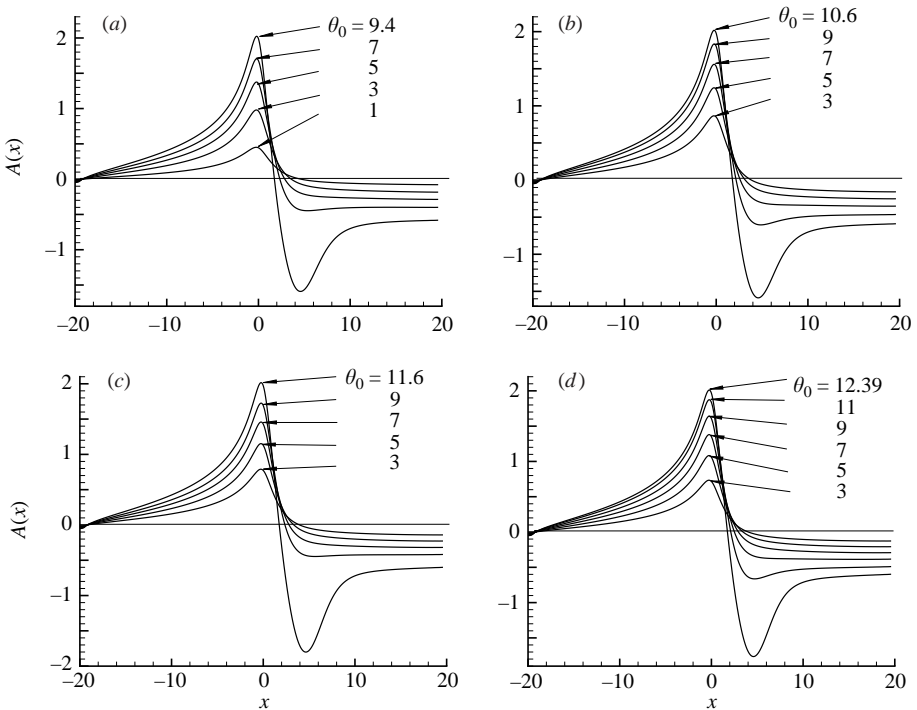FIGURE 11. As for figure 10, but for a compression ramp.

FIGURE 12. Distribution of the displacement function is presented for different values of the Kármán–Guderley parameter $\mathscr{K}$ for the case of expansion ramp. In each figure, numerical results also are presented for several different ramp angles. (*a*) $A(x)$ for $\mathscr{K} = 0$, (*b*) 1, (*c*) 2, (*d*) 3.
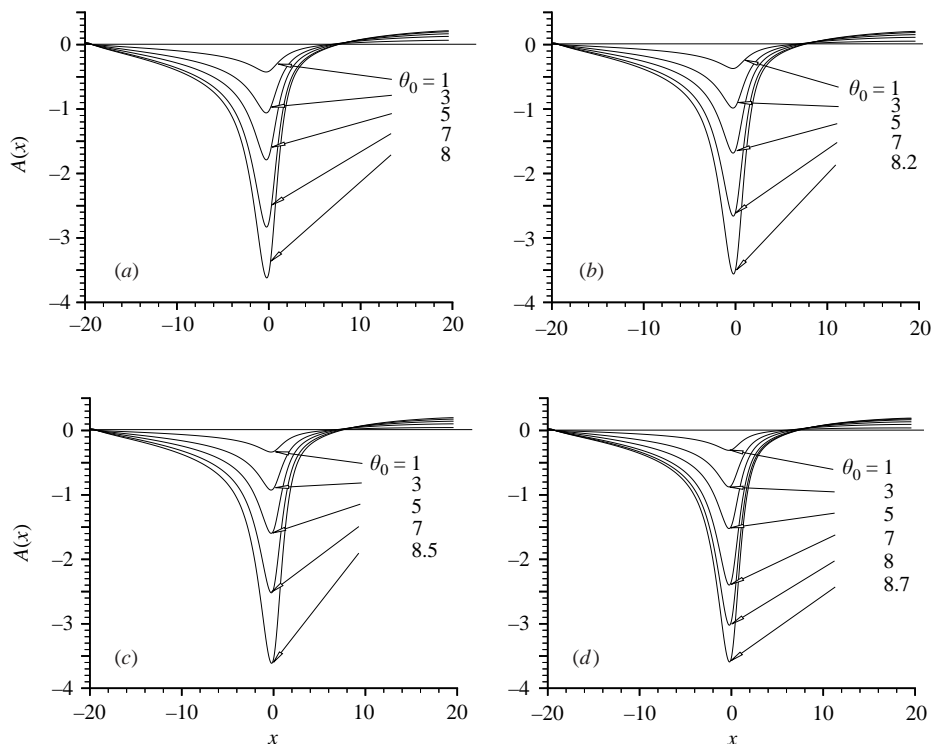
FIGURE 13. As for figure 12, but for a compression ramp.

case, the entire region of recirculating flow is located above the corner. The streamline pattern for $\mathcal{K} = 0$ and $\theta_0 = 8.0$ is shown in figure 6(b).

As can be seen from figure 7, the onset of separation occurs when θ_0 reaches the value $\theta_0 = 6.7$ for $\mathcal{K} = 0$ as shown in figure 6(b). Figures 11(a) and 13(a) show the corresponding distributions of the skin friction and the displacement function for $\mathcal{K} = 0$. The remaining graphs in this paper show the same behaviour for different values of the Kármán–Guderley parameter $\mathcal{K}$, as explained above. However, as $\mathcal{K}$ increases, the incipient separation appears for the greater values of ramp angle θ_0.

The calculations carried out by the current method are based on the use of iterations which inevitably become divergent as soon as the region of recirculating flow is sufficiently large. Unfortunately, we have not been able to calculate the flow properties for very large values of θ_0. For example, the largest θ_0 for $\mathcal{K} = 0.0$ was $\theta_0 = 9.4$ in the case of an expansion ramp. We believe that the reason for this is possibly the non-uniqueness of the solution.

6. Concluding remarks

The properties of a laminar boundary layer near the corner point of a rigid body with a stream of transonic flow have been investigated in the large-Reynolds-number limit. A new numerical technique which is an extension of the so-called semi-inverse method (Carter 1978, 1979; Le Balleur 1978) to calculate the flow field of the laminar separation near the corner point in transonic speeds has been developed based on the viscous–inviscid interaction theory. The method is fully implicit and consists

of the solution of the inviscid transonic flow equation coupled with the boundary-layer solution. In addition to this method, a theoretical analysis of the inviscid transonic flow near the corner point has been performed in the hodograph plane. As a result, far-field boundary conditions have been formulated. Then the boundary layer has been investigated based on the triple-deck scheme. It is shown that the Blasius boundary-layer flow in the vicinity of the sharp corner can be resolved into a triple-deck structure similar to that proposed by Stewartson (1970), the difference being that the scaling laws are altered when the external inviscid flow is transonic. The structure of the triple deck in this case was like that given by Bodonyi (1979) for the related problem of transonic laminar boundary flow near convex corners. However, unlike in the case of Bodonyi (1979) where the solution is considered for the supercritical velocities, the solution of the interaction problem is presented for different values of the Kárman–Guderley parameter corresponding to the subcritical velocities. Emergence of the supersonic zone depending on the ramp angle is observed in the external subsonic flow field although it is small. It has been found that the incipient separation appears for the greater values of ramp angle, as the Kárman–Guderley parameter increases. As a result of the small-scale separation, a region of recirculating flow has been formed in the boundary layer downstream of the corner and the development of the 're-attachment' has been observed for growing ramp angle.

Appendix A. Inspection analysis

The asymptotic form of the triple-deck structure can be obtained by performing the so-called inspection analysis of the flow as follows. As the fluid particles in the interaction region experience extreme acceleration caused by the singular pressure gradient, we have to expect that the convective terms on the left-hand side of the longitudinal momentum equation are of the same order of magnitude as the pressure gradient on the right-hand side. This may be expressed as

$$\rho u \frac{\partial u}{\partial x} \sim \frac{\partial p}{\partial x}. \tag{A 1}$$

In the sublayer (lower deck) $\Delta u \sim u$, and if the aerofoil surface is not artificially heated or cooled, the non-dimensional density ρ and viscosity μ are order-one quantities. This simplifies (A 1), written in finite difference form and yields

$$\Delta u \sim \sqrt{\Delta p}. \tag{A 2}$$

In the boundary layer immediately upstream of the interaction regions, u is of the order of Y. This relation may be written in terms of the 'original' transverse variable $y \sim Re^{1/2}Y$ as

$$\Delta u \sim u \sim Re^{1/2}y. \tag{A 3}$$

On the aerofoil surface the no-slip condition has to be satisfied. This requires the lower deck be viscous. Taking this into account, we suppose that in this region convective terms and viscous terms have to be of the same order of magnitude, i.e.

$$\rho u \frac{\partial u}{\partial x} \sim \frac{1}{Re} \frac{\partial}{\partial y} \left(\mu \frac{\partial u}{\partial y} \right). \tag{A 4}$$

$\Omega_{i,j}^{n-1}$	$\widetilde{\Omega}_{i,j}^{n-1}$	Operator
> 0	> 0	Elliptic
< 0	< 0	Hyperbolic
< 0	> 0	Sonic
> 0	< 0	Shock

TABLE 1. The rules of switching the operators.

In terms of finite-difference operators, this relation may be written as

$$\frac{u}{\Delta x} \sim \frac{1}{Re\, y^2}. \tag{A 5}$$

In addition to these equations, it is known that in the transonic small-disturbance theory, the pressure perturbations introduced in the upper deck may be estimated as

$$\Delta p \sim (\theta^*)^{2/3}, \tag{A 6}$$

where θ^* is the angle of the velocity vector at the outer edge of the boundary layer (see Cole & Cook 1986). It can be estimated as

$$\theta^* \sim \frac{y}{\Delta x}. \tag{A 7}$$

Combining (A 6) and (A 7) we have

$$\Delta p \sim \left(\frac{y}{\Delta x}\right)^{2/3}. \tag{A 8}$$

Solving (A 2), (A 3), (A 5) and (A 8) together, we have found the following estimate for the longitudinal extent of the interaction region

$$x \sim Re^{-3/10}. \tag{A 9}$$

Substituting (A 9) into (A 3) and (A 5) indicates that the thickness of the viscous sublayer

$$y \sim Re^{-3/5}.$$

A rigorous asymptotic analysis of the flow in the three layers of the triple-deck inter-action region can be performed based on this scaling.

Appendix B. Numerical method

B.1. *The external flow*

We calculated at each point two values of $\mathcal{K} - (\phi_x)_{i,j}$ using the central and backward finite-difference approximation for $(\phi_x)_{i,j}$;

$$\Omega_{i,j}^{n-1} = \mathcal{K} - \frac{\phi_{i+1,j} - \phi_{i-1,j}}{2\Delta x}, \qquad \widetilde{\Omega}_{i,j}^{n-1} = \mathcal{K} - \frac{3\phi_{i,j} - 4\phi_{i-1,j} + \phi_{i-2,j}}{2\Delta x}.$$

Here the upper index $n-1$ was used to indicate that $\Omega_{i,j}^{n-1}$ and $\widetilde{\Omega}_{i,j}^{n-1}$ were calculated using a distribution of $\phi_{i,j}$ on the previous iteration. Then the finite-difference operator for equation (4.4) was chosen according to table 1 as in Cole & Cook (1986).

If $\Omega_{i,j}^{n-1} \geqslant 0$ and $\widetilde{\Omega}_{i,j}^{n-1} \geqslant 0$ then equation (4.4) is 'locally' elliptic and should be approximated using central differences for both the second-order derivatives of ϕ. If,

on the other hand, $\Omega_{i,j}^{n-1} < 0$ and $\widetilde{\Omega}_{i,j}^{n-1} < 0$, then a hyperbolic stencil with upstream differencing for ϕ_x and ϕ_{xx} should be used. In our calculations, second-order accurate approximation was adopted. If $\Omega_{i,j}^{n-1} < 0$ and $\widetilde{\Omega}_{i,j}^{n-1} > 0$, then a parabolic stencil should be used. Finally, if $\Omega_{i,j}^{n-1} \geqslant 0$ and $\widetilde{\Omega}_{i,j}^{n-1} < 0$, then the grid point (x_i, y_j) is assumed to lie on a shock wave and we therefore used for such points the same stencil as in the case of the elliptic points.

It follows that the coefficients in (4.7) may be calculated as

$$a_j = \frac{1}{(\Delta\bar{y})^2}, \quad c_j = \frac{1}{(\Delta\bar{y})^2} \quad \text{for all cases,}$$

$$b_j = \begin{cases} -\Omega_{i,j}^{n-1}\dfrac{1}{(\Delta x)^2} - \dfrac{1}{(\Delta\bar{y})^2} & \text{if elliptic and shock,} \\[2mm] \widetilde{\Omega}_{i,j}^{n-1}\dfrac{1}{(\Delta x)^2} - \dfrac{1}{(\Delta y)^2} & \text{if hyperbolic,} \\[2mm] -\dfrac{1}{(\Delta\bar{y})^2} & \text{if sonic,} \end{cases}$$

$$d_j = \begin{cases} \Omega_{i,j}^{n-1}\dfrac{\phi_{i+1,j} + \phi_{i-1,j}}{(\Delta x)^2} & \text{if elliptic and shock,} \\[2mm] \widetilde{\Omega}_{i,j}^{n-1}\dfrac{-5\phi_{i-1,j} + 4\phi_{i-2,j} - \phi_{i-3,j}}{(\Delta x)^2} & \text{if hyperbolic,} \\[2mm] 0 & \text{if sonic.} \end{cases}$$

Note that $\phi_{i-1,j}$, $\phi_{i-2,j}$ and $\phi_{i-3,j}$ have been updated already, while $\phi_{i+1,j}$ should be taken from the previous iteration.

The Thomas technique was proved to be an efficient tool for solving (4.7) on each mesh line $x = x_i$. Two boundary conditions are required to solve (4.7). At the top boundary, the value of ϕ_{i,J_m} as given by the boundary condition (3.18) was used. At the bottom boundary, $\phi_{i,0}$ has been calculated using the second boundary condition in (3.9), i.e.

$$\frac{\partial\phi}{\partial y} = -A(x) + f'(x) \quad \text{at} \quad y = 0,$$

which may be written in finite differences as

$$\frac{-3\phi_{i,0} + 4\phi_{i,1} - \phi_{i,2}}{2\Delta\bar{y}} = -A'(x_i) + f'(x_i) \qquad (i = 1, \ldots, I_{m-1}). \tag{B 1}$$

As has been mentioned already, (4.7) may be solved on each mesh line $x = x_i$ using the Thomas reduction formula

$$\phi_{i,j} = R_j\phi_{i,j-1} + Q_j. \tag{B 2}$$

In particular, for $j = 1$ and $j = 2$ we have

$$\phi_{i,1} = R_1\phi_{i,0} + Q_1,$$
$$\phi_{i,2} = R_2\phi_{i,1} + Q_2 = R_1R_2\phi_{i,0} + R_2Q_1 + Q_2. \tag{B 3}$$

Substituting (B 3) into (B 1) and solving for $\phi_{i,0}$ we have

$$\phi_{i,0} = \frac{R_2Q_1 + Q_2 - 4Q_1 + 2\Delta y[-A'(x_i) + f'(x_i)]}{4R_1 - R_1R_2 - 3}. \tag{B 4}$$

Now the distribution of ϕ along the line x_j may be updated using (B 2), and we can move on to the next line. The sweeps over the calculation domain have been repeated as many times as required for the convergence criterion,

$$\max_{i,j} \left| \phi_{i,j}^{new} - \phi_{i,j}^{old} \right| < \epsilon,$$

to be met. The numerical calculations have been performed with $\epsilon = 10^{-6}$. The size of the computational domain has been taken to be $x \in [-20, 20]$, $y \in [0, 15]$ and $x \in [-30, 30]$, $y \in [0, 15]$. The number of grid points have been also varied from 100×50 to 200×100.

B.2. *The internal flow*

If $U_{i,j} \geqslant 0$, then (4.10) should be approximated using backward finite differences for the first-order derivative of ω with respect to x. If, on the other hand $U_{i,j} < 0$, the forward finite differencing for $\partial \omega / \partial X$ should be used. Also, in our calculations second-order, accurate approximation was adopted.

It follows that the coefficients in (4.15) may be calculated as

$$a_j = \frac{V_{i,j}}{2\Delta y} - \frac{1}{(\Delta y)^2},$$

$$b_j = \begin{cases} \dfrac{3U_{i,j}}{2\Delta x} + \dfrac{2}{(\Delta y)^2} & \text{if } U_{i,j} \geqslant 0, \\[2mm] -\dfrac{3U_{i,j}}{2\Delta x} + \dfrac{2}{(\Delta y)^2} & \text{if } U_{i,j} < 0, \end{cases}$$

$$c_j = -\frac{1}{(\Delta y)^2} - \frac{V_{i,j}}{2\Delta y},$$

$$d_j = \begin{cases} \dfrac{2U_{i,j}}{\Delta x}\omega_{i+1,j} - \dfrac{U_{i,j}}{2\Delta x}\omega_{i+2,j} & \text{if } U_{i,j} \geqslant 0, \\[2mm] -\dfrac{2U_{i,j}}{\Delta x}\omega_{i-1,j} - \dfrac{U_{i,j}}{2\Delta x}\omega_{i-2,j} & \text{if } U_{i,j} < 0. \end{cases}$$

The Thomas technique proved to be an efficient tool for solving (4.15) on each mesh line $x = x_i$. Two boundary conditions are required to solve (4.15). At the top boundary, the value of $\omega_{i,J_m} = 1$ given by the boundary condition (4.12) was used. At the bottom boundary, $\omega_{i,0}$ was calculated based on following procedure.

We write the formula to calculate $\omega_{i,j}$ as

$$\omega_{i,j} = R_j \omega_{i,j-1} + Q_j \text{ for } j = 0, 1, 2, \ldots, J_m, \tag{B 5}$$

where $R_{j_m} = 0$ and $Q_{J_m} = 1$, and also $\omega_{i,j}$ can be calculated as

$$\omega_{i,j} = \tilde{A}_j \omega_{i,0} + \tilde{B}_j, \tag{B 6}$$

where $\tilde{A}_0 = 1$ and $\tilde{B}_0 = 0$. A general formula to calculate $\tilde{A}_j$ and $\tilde{B}_j$ for $j \geqslant 1$ may be easily derived substituting $\omega_{i,j-1} = \tilde{A}_{j-1}\omega_{i,0} + \tilde{B}_{j-1}$ into (B 5). This yields

$$\tilde{A}_j = \tilde{A}_{j-1} R_j, \quad \tilde{B}_j = R_j \tilde{B}_{j-1} + Q_j. \tag{B 7}$$

Combining (3.7*b*) with (4.14) and discretization gives

$$y_{max} + A_i = \sum_{j=1}^{J_m} \frac{\omega_{i,j} + \omega_{i,j-1}}{2} \Delta y, \tag{B 8}$$

where A_i is the value of the displacement function, $A(x)$, evaluated at $x = x_i$. Using (B 6), we rearrange (B 8) and we have

$$\omega_{i,0} = \frac{1}{D}(A_i + y_{max} - C), \qquad (B\,9)$$

$$\text{where} \quad C = \tfrac{1}{2}\Delta y \sum_1^{J_m}(\tilde{A}_j + \tilde{A}_{j-1}), \quad D = \tfrac{1}{2}\Delta y \sum_1^{J_m}(\tilde{B}_j + \tilde{B}_{j-1}).$$

Now it is easy to update the distribution of ω on the line considered by making use of (B 6). This procedure has been repeated as many times as required for the convergence criterion,

$$\max_{i,j} \left| \omega_{i,j}^{new} - \omega_{i,j}^{old} \right| < \text{tolerance},$$

to be met. The tolerance has been taken to be 10^{-6}. The typical size of the computational domain was $x \in [-20, 20]$, $y \in [0, 15]$. The number of grid points was also varied from 50×50 to 200×100.

REFERENCES

ABRAMOWITZ, M. & STEGUN, I. A. 1965 *Handbook of Mathematical Functions, with Formulas, Graphs, and Mathematical Tables*. National Bureau of Standards.

BODONYI, R. J. 1979 Transonic laminar boundary-layer flow near convex corners. *Q. J. Mech. Appl. Maths* **32**, 63–71.

BODONYI, R. J. & KLUWICK, A. 1977 Freely interacting transonic boundary layers. *Phys. Fluids* **20**, 1432–1437.

BODONYI, R. J. & KLUWICK, A. 1982 Supercritical transonic trailing-edge flow. *Q. J. Mech. Appl. Maths* **35**, 265–277.

BODONYI, R. J. & KLUWICK, A. 1998 Transonic trailing-edge flow. *Q. J. Mech. Appl. Maths* **51**, 297–310.

CARTER, J. 1978 A new boundary layer interaction technique for separated flows. NASA *TM*-78690.

CARTER, J. 1979 A new boundary-layer inviscid iteration technique for separated flow. *AIAA Paper* 79–1450.

COLE, J. D. & COOK, L. P. 1986 *Transonic Aerodynamics*. North-Holland.

JENSON, R., BURGGRAF, O. & RIZZETTA, D. 1975 Asymptotic solution for supersonic viscous flow past a compression corner. *Lecture Notes in Physics*, vol. 35, pp. 218–224. Springer.

LE BALLEUR, J. 1978 Couplage visqueux–non-visqueux; méthode numérique et applications aux écoulements bidimensionnels transoniques et supersoniques. *Rec. Aerosp.* **2**, 65–76.

NEILAND, V. Y. 1971 The asymptotic theory of the interaction of a supersonic flow with a boundary layer. *Izv. Akad. Nauk SSSR, Mech. Zhid. i Gaza* 4, 41–47 (engl. transl. *Fluid Dyn.* **6**, 587–592).

RUBAN, A. I. 1976 On the theory of laminar flow separation of a fluid from a corner point on a solid surface. *Uch. Zap. TsAGI* **7** (4) 18–28 (in Russian).

RUBAN, A. I. 1978 Numerical solution of the local asymptotic problem of the unsteady separation of a laminar boundary layer in a supersonic flow. *Z. Vych. Mat. Mat. Fiz.* **18**, 1253–1265 (engl. transl. *USSR Comput. Maths Math. Phys.* **18** (5), 175–187).

RUBAN, A. I. & TÜRKYILMAZ, I. 2000 On laminar separation at a corner point in transonic flow. *J. Fluid Mech.* **423**, 345–380.

STEWARTSON, K. 1970 On supersonic laminar boundary layers near convex corners. *Proc. R. Soc. Lond.* A **319**, 289–305.